

**Influence of different Heat Treatments on the microstructural Evolution and  
Microhardness of Laser Powder Bed Fusion manufactured Inconel 625**

by

Jan Lieben

A thesis submitted to the Graduate Faculty of  
Auburn University  
in partial fulfillment of the  
requirements for the Degree of  
Master of Science

Auburn, Alabama  
August 8, 2020

Keywords: Laser Powder Bed Fusion (L-PBF), Inconel 625, Delta-phase

Copyright 2020 by Jan Lieben

Approved by

Barton C. Prorok, Chair, Mechanical Engineering  
Dong-Joo Kim, Alumni Professor, Mechanical Engineering  
Xiaoyuan Lou, Associate Professor, Mechanical Engineering

## Abstract

Laser Powder Bed Fusion is an additive manufacturing technology that allows the production of parts with complex geometries. [8] The high energy focused laser beam that selectively melts the cold powder bed leads to high cooling rates which result in a fine microstructure and is often accompanied by internal stresses which may require a stress relief heat-treatment. Manufacturer recommended heat treatments are often based on the nominal powder composition and do not include the L-PBF produced microstructure. Inconel 625, a nickel-based superalloy, is frequently used for L-PBF processes. One of the major concerns is the precipitation of  $\delta$ -phase at elevated temperatures, which has almost exclusively detrimental effects on the material's mechanical properties. This thesis investigates the influence of heat treatments at 700 °C, 900 °C and 1050 °C for one and two hours on the microstructure and microhardness of the manufactured parts and shows that the secondary phases are hard to detect, that the change in lattice parameter can be used to indirectly show the nature of secondary phase formation and that a post-processing heat treatment should be carefully chosen in order to not be ineffective or even detrimental to the part's performance.

## Table of Contents

Abstract .....	2
Table of Contents .....	3
List of Tables .....	5
List of Figures .....	6
List of Abbreviations.....	8
1 Introduction .....	9
1.1 Laser Powder Bed Fusion.....	9
1.2 Cooling rates.....	13
1.3 Inconel 625 .....	13
2 Materials and Methods .....	18
2.1 L-PBF machine .....	18
2.2 Sample Preparation .....	19
2.3 Heat Treatments .....	20
2.4 Hardness and Microstructure.....	21
3 Results and Discussion.....	24
3.1 Microhardness of the one-hour heat-treated specimen .....	24
3.2 Microstructure of the one-hour heat-treated specimen .....	25
3.3 Microhardness of the two-hour heat-treated specimen .....	31
3.4 Microstructure of the two-hour heat-treated specimen .....	32

3.5	Comparison between both heat treatments.....	36
4	Conclusion and outlook.....	38

## List of Tables

Table 1: Limiting Chemical Composition of INCONEL 624, % according to UNS N06625 .....	14
Table 2: Sample designation, orientation and heat treatments .....	21
Table 3: Variation in lattice parameter calculated from (200) peak position for L-PBF manufactured IN625 in 4 different conditions for the one-hour heat treatment.....	30
Table 4: Variation in lattice parameter calculated from (200) peak position for L-PBF manufactured IN625 in 4 different conditions for the two-hour heat treatment.....	35

## List of Figures

Figure 1: Schematic of the L-PBF technology [11].....	11
Figure 2: Overview of relationship between input parameters and underlying physics of metal AM [2].....	12
Figure 3: A time-temperature-transformation (TTT) diagram comparing the presence of $\delta$ -phase in additively manufactured IN625 to the wrought material. The dashed lines estimate approximately 1 %-volume fraction of $\delta$ -phase. [20] .....	15
Figure 4: Time-Temperature-Transformation Diagram of IN625 [15].....	16
Figure 5: SE micrograph and elemental X-ray maps of as-built IN625 sample [6] .....	17
Figure 6: Picture of the Concept Laser MLab Cusing 100R L-PBF machine used for all AM processes.....	19
Figure 7: Arrangement of the manufactured INC625 cubes on the built plate .....	20
Figure 8: Schematic explaining Bragg’s Law .....	22
Figure 9: Sketch of a Vickers indenter [10] .....	23
Figure 10: Microhardness (Vickers, 1000 gf, 30 s) of vertical and diagonal INC625 samples, for the as-built condition and three different heat-treated samples at 700 °C, 900 °C and 1050 °C for one hour each and air-cooled. The gray dashed line shows the hardness of wrought IN625 in non-heat-treated condition.....	25
Figure 11: Microstructure of AM INC625 a) As-built condition, b) heat treated at 700°C for 1 hour, air cooled, c) heat treated at 900 °C for 1 hour, air cooled, d) heat treated at 1050 °C for 1 hour, air cooled. ....	27

Figure 12: XRD results of the IN625 vertical as built specimen in the 2-theta range from 5° to 100°.....28

Figure 13: XRD results of the IN625 vertical specimen in the as built condition and heat treated for one hour at three different temperatures in the 2-theta range from 5° to 100° .....29

Figure 14: (200) Peak shift for L-PBF manufactured In625 in four different heat treatment conditions .....31

Figure 15: Microhardness (Vickers, 1000 gf, 30 s) of vertical and diagonal IN625 samples, for the as built condition and three different heat-treated samples at 700°C, 900°C and 1050°C for two hours each and air-cooled. The gray dashed line shows the hardness of the wrought IN625 in non-heat-treated condition.....32

Figure 16: Microstructure of AM INC625 a) heat treated at 700 °C for 2 hours, air cooled, b) heat treated at 900 °C for 2 hours, air cooled, c) heat treated at 1050 °C for 2 hours, air cooled, d) higher magnification of the 700°C heat treated sample, red arrows showing melt pool boundaries, green arrow shows grain growth in built direction. ....33

Figure 17: XRD results of the IN625 vertical specimen in the as built condition and heat treated for two hours at three different temperatures in the 2-theta range from 5° to 100° .....34

Figure 18: (200) Peak shift for L-PBF manufactured In625 in four different heat conditions for the two-hour heat-treated specimen .....36

## List of Abbreviations

AM	Additive manufacturing
CAD	Computer Aided Design
EDS	Energy Dispersive Spectroscopy
FESEM	Field Emission Scanning Electron Microscopy
IN625	Inconel 625
L-PBF	Laser Powder Bed Fusion
OM	Optical Microscopy
TEM	Transmission Electron Microscopy
XRD	X-Ray Diffractometer

## 1 Introduction

Inconel 625 is a solid solution strengthened nickel based super alloy that combines high mechanical properties, corrosion resistance and weldability and is frequently used in additive manufacturing applications. However, the rapid cooling times during most additive manufacturing (AM) processes, e.g. Laser Powder Bed Fusion (L-PBF), result in different microstructures than conventional manufacturing methods and can influence the macroscopic performance. Well investigated heat treatments for IN625 parts that are manufactured by conventional methods may be ineffective or even detrimental for AM manufactured parts, as they are often based on the nominal powder composition which does not include the microstructure of the manufactured parts. This thesis has the goal to manufacture IN625 specimen, expose them to different heat treatments and analyze afterwards the microstructure and the influence on the microhardness to evaluate the effect of different heat treatments.

### 1.1 Laser Powder Bed Fusion

In the last decades, additive manufacturing technologies have attracted more and more interest amongst different industrial sectors due to their unique benefits over a lot of traditional manufacturing techniques. One heavily researched technology amongst these is Laser Powder Bed Fusion, which describes the selective melting and re-solidifying of thin layers of metal powder until the final part geometry is achieved. L-PBF is especially of high interest for fields that require individualized parts as the biomedical sector, or sectors that require complex shapes and structures while still advanced mechanical performance is needed. Additional advantages of Laser Powder Bed Fusion are the reduced material waste, its multifunctional optimization and weight reduction

of manufactured parts. On the downside, only a limited selection of metals and alloys is available for the L-PBF process so far. Furthermore, the processed parts have a high isotropic behavior depending on the built direction. [1],[2]

The Laser Powder Bed Fusion process can be enclosed in three main parts: The design of the component, the built-process and post-processing. [3] For the first step, a 3-Dimensional model of the part is created with a CAD software. The digital copy of the part is then sliced into many slices, while the thickness of each slice represents the layer thickness during the melting later on. The thinner the slice, the higher the resolution but the longer the actual manufacturing process takes. Furthermore, support structures that fix the part to the built plate and dissipate heat are added and the laser scanning paths are set. The part is then manufactured by a repeating process circle. A thin layer of metal powder is distributed over the built plate, before the laser with the pre-distinguished parameters selectively melts only those parts of the powder bed that represent the material of the building component. The built plate is then lowered by the thickness of one layer and the next layer of powder is spread. Figure 1 shows a schematic of a L-PBF process involving the major steps that are mentioned above. [1],[3]

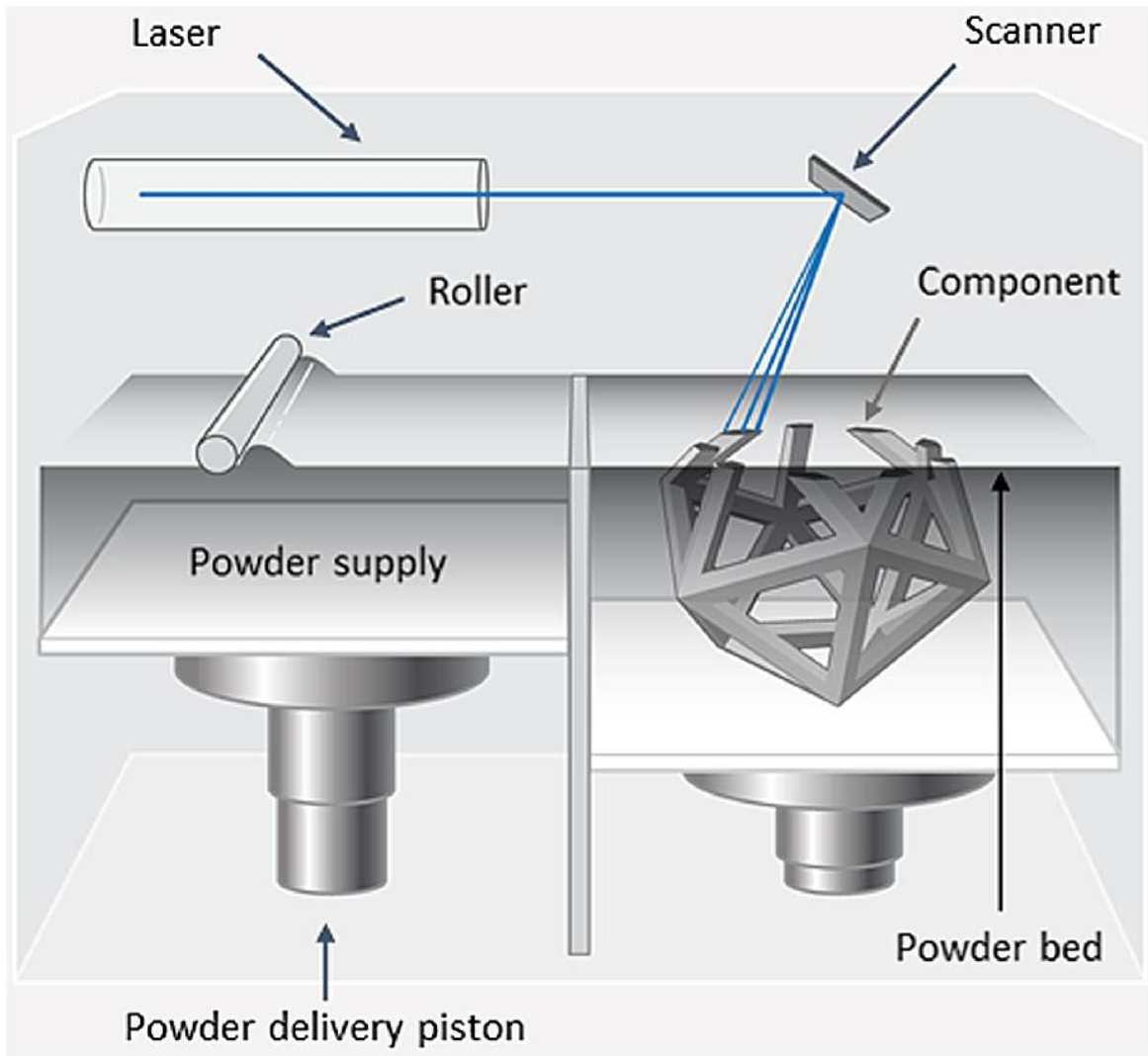


Figure 1: Schematic of the L-PBF technology [11]

A lot of different parameters influence the built job and the outcome of the product. Even though a lot of research has already been done, there are too many different parameters that are correlated to each other and only minor changes of one parameter can have a huge effect on the others, as shown in figure 2. [2] Therefore, for commercial usage of the L-PBF process it is usually essential to keep the processing conditions constant and only change the major parameters. The major parameters that are changed are the Laser Power  $P_L$ , the hatch distance  $h$ , the layer thickness  $d$  and

the scan velocity  $v_s$ , which can all be combined as the energy input according to the following equation:

$$E_v = \frac{P_L}{v_s * h * d}$$

The use of the energy input makes it easier to compare different processes to each other.

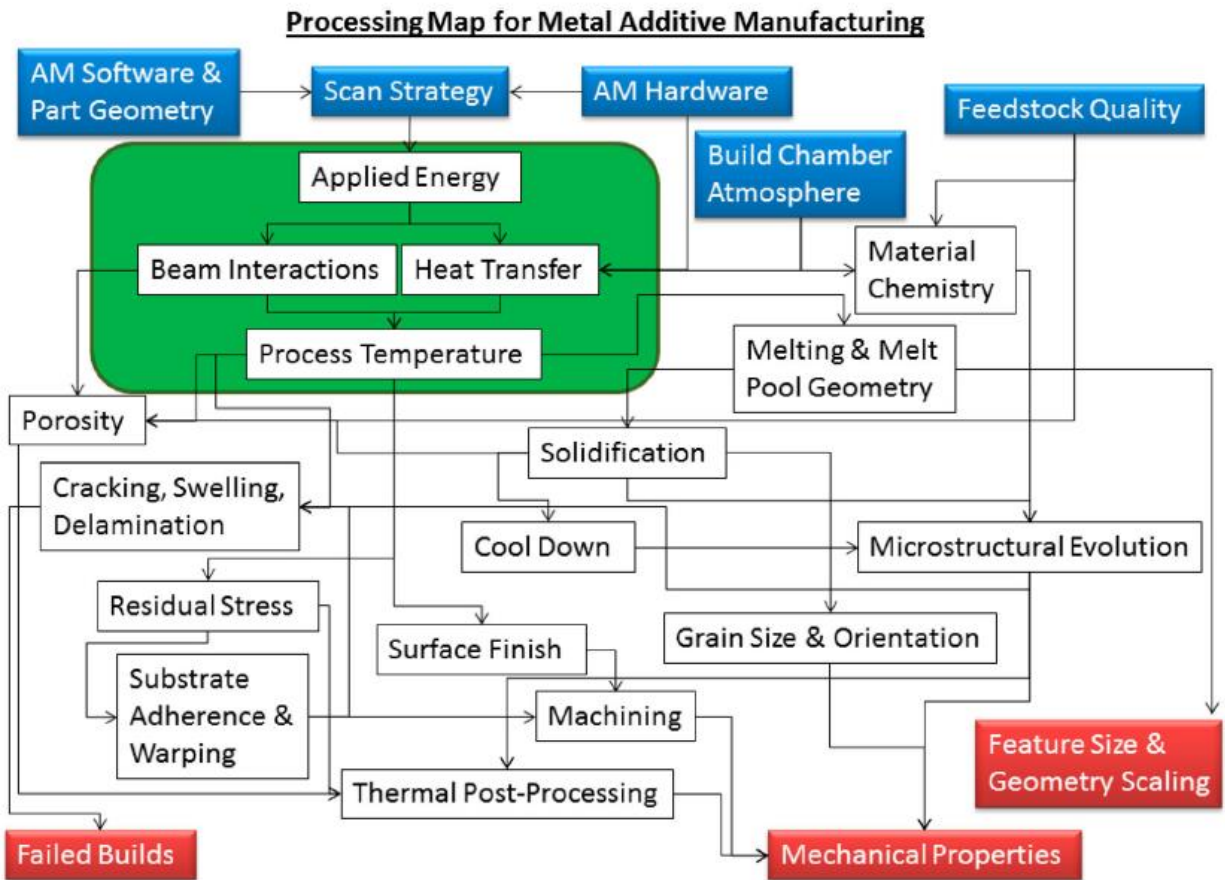


Figure 2: Overview of relationship between input parameters and underlying physics of metal

AM [2]

## 1.2 Cooling rates

A Laser Powder Bed Fusion process is often followed by an annealing process, whether it is to gain the necessary mechanical properties for the manufactured parts or a stress-relief anneal before separating the parts from the built plate. Conventional manufacturing processes usually have much lower cooling rates than additive manufacturing processes, especially L-PBF, because of the high localized energy input surrounded by the comparably cool surrounding. A typical casting process for alloys shows cooling rates between 1 to 1000 K/s. [5] Even after a homogenization process, cast alloys sometimes show remains of the solidified microstructure. Wrought processes usually result in very uniform microstructures. AM processes on the other hand have cooling rates in the order of  $10^3$  to  $10^6$  K/s. This usually results in a finer dendrite structure with much smaller primary dendrite spacing. The obtained microstructure often results in inconsistent properties that sometimes differ from those of wrought materials, even though the nominal composition is the same. Kreitzberg et al. have reported that the mechanical properties of L-PBF and wrought IN625 are comparable, but the elongation to failure at elevated temperatures was found to be less than half. [8]

## 1.3 Inconel 625

Inconel 625 is a solid-solution strengthened nickel-based superalloy which is frequently used for several emerging industries, as the medical or aerospace sectors due to its desirable mechanical properties, corrosion resistance and its capability to work at elevated temperatures. In addition, IN625 exhibits good weldability and fabricability which makes it even more attractive for additive manufacturing as it allows to manufacture complex shapes that do not require a lot of post-processing. Table 1 shows the composition of Inconel 625.

Table 1: Limiting Chemical Composition of INCONEL 624, % according to UNS N06625

Element	Ni	Cr	Fe	Mo	Nb	C
%	58.0 min.	20.0-23.0	5.0 max.	8.0-10.0	3.15-4.15	0.10 max.
Element	Si	P	S	Al	Ti	Co
%	0.5 max.	0.015 max.	0.015 max.	0.40 max.	0.40 max.	1.0 max.

The materials strength is traced back to the solid solution strengthening of Cr, Mo and Nb. Further strengthening is reported to be due to the precipitation of the metastable  $\text{Ni}_3\text{Nb}$   $\gamma''$ -phase. The equilibrium phase is the  $\text{Ni}_3\text{Nb}$   $\delta$ -phase, which especially forms at elevated temperatures (above 750 °C) where the  $\gamma''$ -phase dissolves. However, as  $\delta$  is the equilibrium phase, given enough time it will eventually form after long enough time. For conventional manufactured IN625 parts that are in use at elevated temperatures, it takes hundreds to thousands of hours until  $\gamma''$  or  $\delta$  precipitate. [8] While  $\gamma''$  may be desirable due to its strengthening effects,  $\delta$  is almost always detrimental to the mechanical properties and should be avoided or kept to a small fracture. Figure 3 shows the thermal exposure conditions for  $\delta$  formation in additively manufactured IN625 compared to wrought IN625, figure 4 shows the complete TTT diagram for IN625.

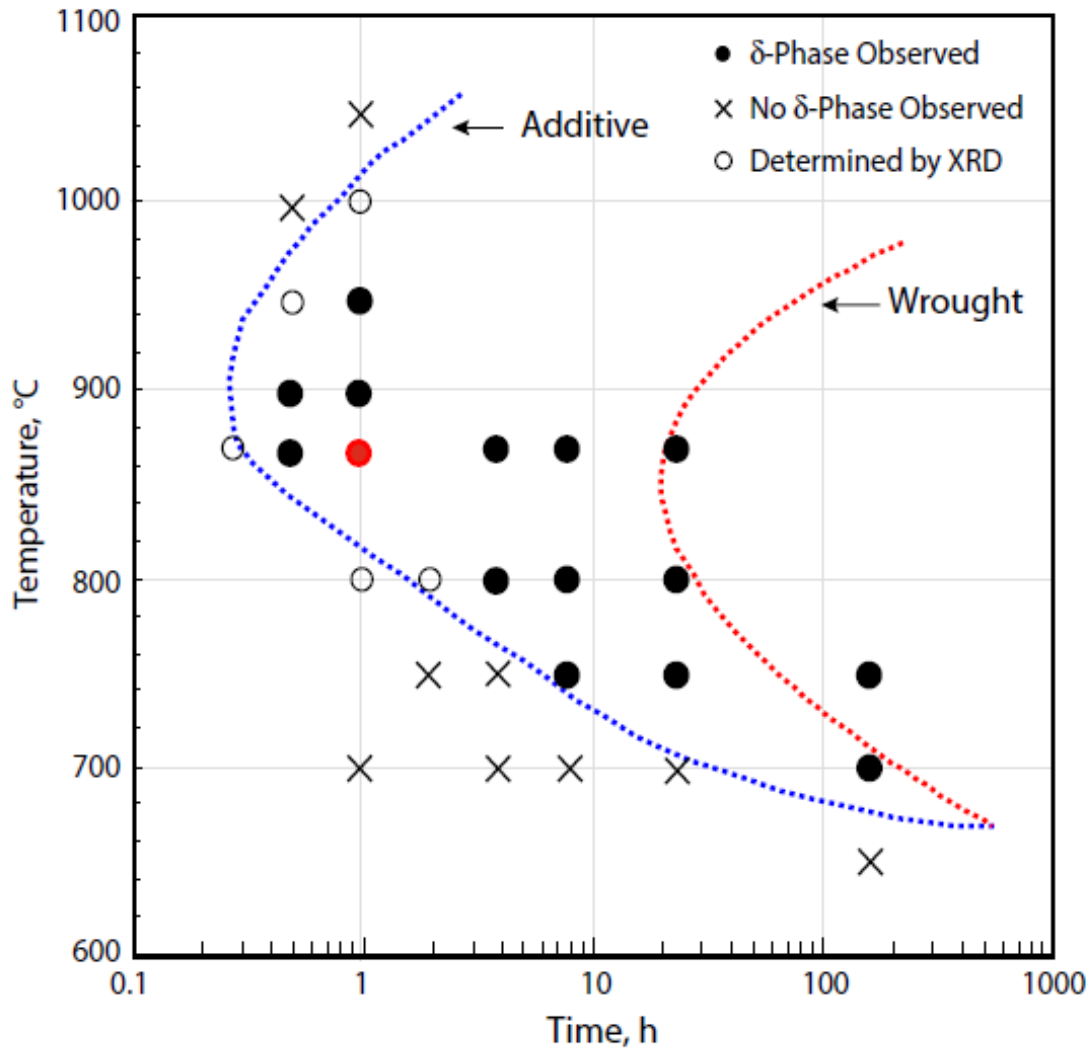


Figure 3: A time-temperature-transformation (TTT) diagram comparing the presence of  $\delta$ -phase in additively manufactured IN625 to the wrought material. The dashed lines estimate approximately 1 %-volume fraction of  $\delta$ -phase. [20]

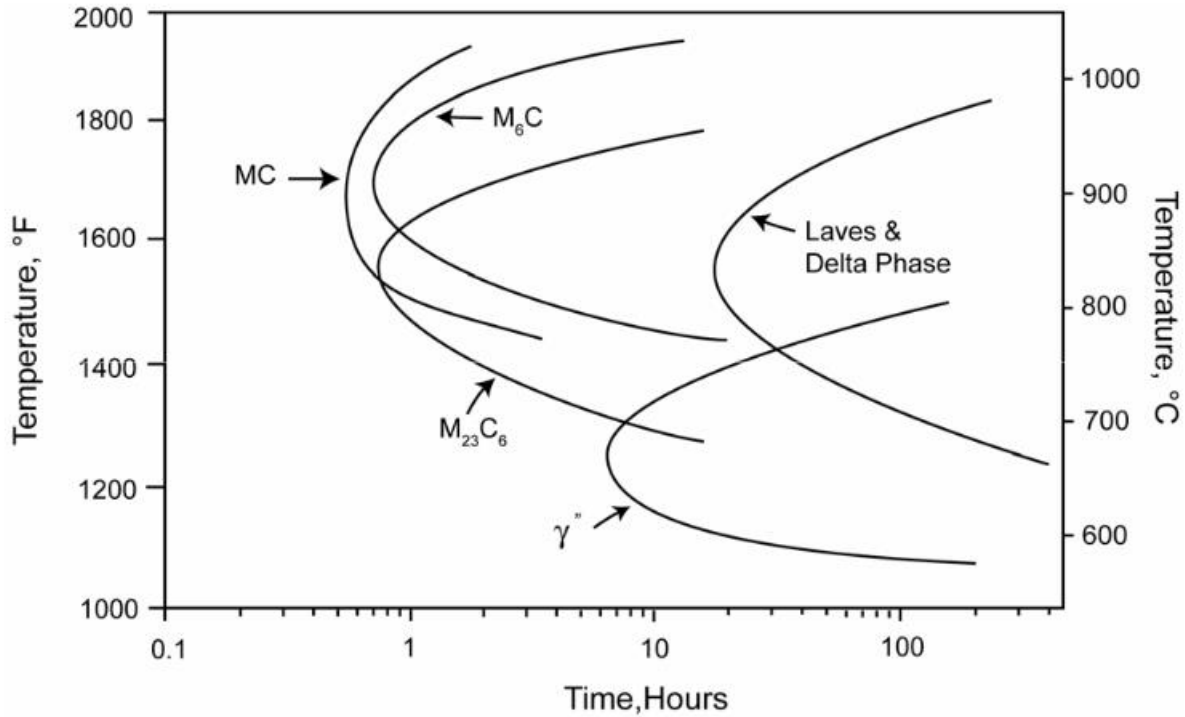


Figure 4: Time-Temperature-Transformation Diagram of IN625 [15]

As it can be seen, the time for  $\delta$  formation for the same temperature is drastically reduced for additive manufacturing compared to wrought processes. This behavior can be explained by the segregation of solute elements during the solidification, which increases the probability for secondary phase formation, as  $\delta$ . During Laser Powder Bed Fusion the cooling rate is much higher compared to conventional processes. This is known to lead to a finer dendritic structure with smaller dendrite spacing, as explained above. [5] Zhang et al. showed that L-PBF produces a finer microstructure for IN625 than other AM processes (EBM and L-DMD) and that the cellular/columnar dendrites are enriched in Mo and Nb, while Ni and Cr are deficient, as can be seen in figure 5, which shows the SE micrograph and elemental X-ray maps of an as-built IN625 sample. [6]

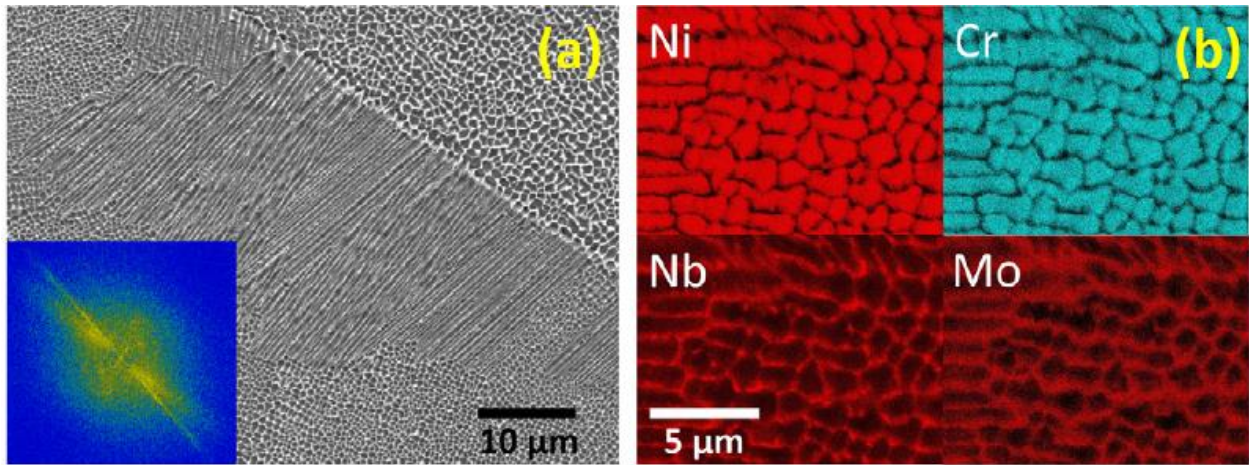


Figure 5: SE micrograph and elemental X-ray maps of as-built IN625 sample [6]

The enrichment in the substructures rather than a homogeneous microstructure is expected to be the primary reason for faster secondary phase precipitation in L-PBF processes compared to conventional manufacturing processes. [6]

## 2 Materials and Methods

In this chapter the materials and methods that are used to produce the required specimen, perform different heat treatments and carry out the microstructural characterization are introduced. The standard testing methods that are used are briefly explained. The used process parameters as well as the L-PBF machine are presented. Machines and methods to examine the microstructure and hardness as well as to carry out the heat treatments are demonstrated.

### 2.1 L-PBF machine

A Concept Laser MLab Cusing 100R that is used to produce all AM parts that are necessary is shown in figure 6. Since 2016, Concept Laser is a part of GE additive, a division of General Electric. [9] The AM machine is equipped with a 100 W fiber laser that has a wavelength of 1070 nm. The build volume of the machine measures 90 x 90 x 80 mm.



Figure 6: Picture of the Concept Laser MLab Cusing 100R L-PBF machine used for all AM processes

## 2.2 Sample Preparation

A total of 24 cubes with the dimensions  $10 \times 10 \text{ mm}^2$  have been additively manufactured. The laser power is set to 90 W with a scan speed of 800 mm/s. The laser diameter is  $80 \text{ }\mu\text{m}$  and the layer thickness is set to  $25 \text{ }\mu\text{m}$ . These parameters have been evaluated by co-workers in a previous work to produce IN625 of high density and good surface morphology. As shown in figure 7, half of the cubes have been built in a vertical orientation on the built plate, the other half rotated by  $45^\circ$ . In the further course of this thesis, vertical samples have the abbreviation V, diagonal ones D.



Figure 7: Arrangement of the manufactured INC625 cubes on the built plate

### 2.3 Heat Treatments

After separating the specimen from the built plate, one of each orientation is exposed to a different heat treatment. The first two cubes are kept as the as-built specimen, the next two are heat treated at 700 °C for one hour, the next two at 900 °C for one hour and two at 1050 °C for one hour. The same heat treatments are conducted to samples for two hours. All samples are air cooled. Following the heat treatment, the samples are sectioned parallel to the built direction and undergo standard metallographic preparation including grinding and polishing. Table 2 lists all specimen, their short names and the different heat treatments.

Table 2: Sample designation, orientation and heat treatments

Name	As-built_V	700°C_1h_V	900°C_1h_V	1050°C_1h_V	As-built_D	700°C_1h_D	900°C_1h_D
Orientation	vertical	vertical	vertical	vertical	diagonal	diagonal	diagonal
Heat treatment	none	700°C, 1h	900°C, 1h	1050°C, 1h	none	700°C, 1h	900°C, 1h
Name	1050°C_1h_D	700°C_2h_V	900°C_2h_V	1050°C_2h_V	700°C_2h_D	900°C_2h_D	900°C_2h_D
Orientation	diagonal	vertical	vertical	vertical	diagonal	diagonal	diagonal
Heat treatment	1050°C, 1h	700°C, 2h	900°C, 2h	1050°C, 2h	700°C, 2h	900°C, 2h	900°C, 2h

## 2.4 Hardness and Microstructure

Subsequent to the heat treatments an X-ray diffraction of every specimen is performed. A Bruker D8 Diffractometer (XRD) with a copper X-ray source is used. The working voltage for diffraction used is 40 kV with a current of 40 mA. The obtained diffraction patterns are compared to reported diffractograms from the literature.

X-ray diffraction uses incident X-ray waves, here Copper K- $\alpha$  with a wavelength of 1.5406 Å, to radiate the examination target. The target's electrons elastically scatter the X-rays and most of them disappear due to destructive interference. However, as most materials have a repeating crystal structure, some X-rays are scattered constructive and add up to a repeating signal, as shown in figure 8. The path difference of two, or more, parallel waves create reflection spots in a pattern when the path difference equals any integer multiple of  $\lambda$ . This allows to calculate the spacing between two diffraction planes according to Bragg's Law:

$$2d_{hkl}\sin\theta = n\lambda$$

By using simple geometry and knowledge about crystal structures, the miller indices and lattice parameters can be calculated.

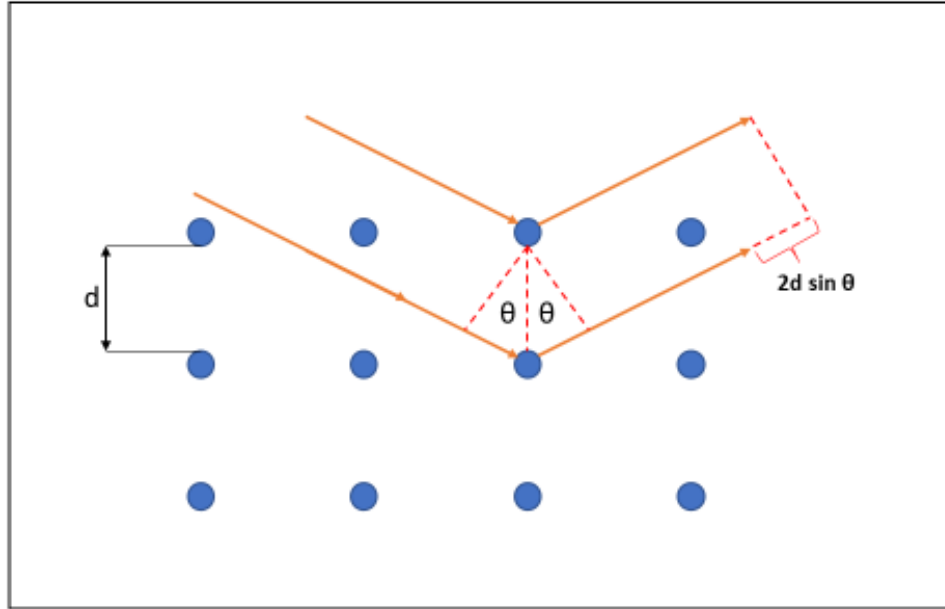


Figure 8: Schematic explaining Bragg's Law

Following XRD, the Vickers hardness is measured. All hardness measurements are conducted on a Leco DM-400 hardness tester with an applied load of 1000 gf (1 kgf = 9.8 N) for 30 seconds. For a Vickers hardness test, a square-based pyramidal shaped indenter, made of diamond, with face angles of  $136^\circ$ , as shown in figure 9, is used. After applying a force with the indenter onto the specimen, a light microscope is used to measure the indentation diagonals. The Vickers hardness number is then calculated, using the following equation:

$$HV = 1.000 \times 10^3 \times P/A_s = 1854.4 \times P/d^2$$

Where P is the force applied in gf,  $A_s$  is the surface area of the indentation in  $\mu\text{m}^2$  and d is the mean diagonal length in  $\mu\text{m}$ . [10]

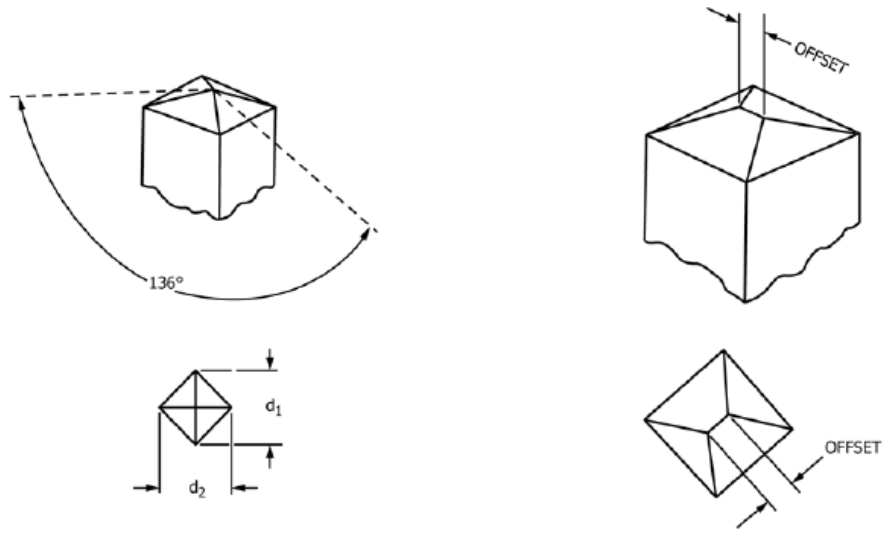


Figure 9: Sketch of a Vickers indenter [10]

Lastly, the samples are etched using Kalling's 2 reagent to visualize the microstructure under an Olympus BX51 optical microscope that is equipped with a DP73 camera.

### 3 Results and Discussion

The following chapter presents the results from the above-mentioned experiments. First, the microhardness measurements for the one-hour heat treatment are presented. Then the XRD results and the microstructure images are presented and evaluated. Afterwards the same is done for the two-hour heat-treated specimen. In the last part a comparison between the one-hour and the two-hour heat-treated specimen is conducted and evaluated.

#### 3.1 Microhardness of the one-hour heat-treated specimen

The microhardness is measured for all specimen. Figure 10 shows the results for the diagonal and vertical specimen that are heat treated for one hour. It can be clearly seen, that the vertical as well as the diagonal sample follow the same trend. The micro hardness increases from the as-built condition slightly when heat treated for one hour at 700 °C ( HV  $361.75 \pm 7.56$ , HV  $362.67 \pm 13.1$  for vertical and diagonal built direction, respectively), before dropping down below the as-built condition for 900 °C and then dropping even further for the 1050 °C condition. Generally, the hardness for vertical and diagonal built orientation are in good agreement, the diagonal built orientation seems to produce slightly higher microhardness. The difference in hardness for the 900 °C heat treatment is more pronounced than the others.

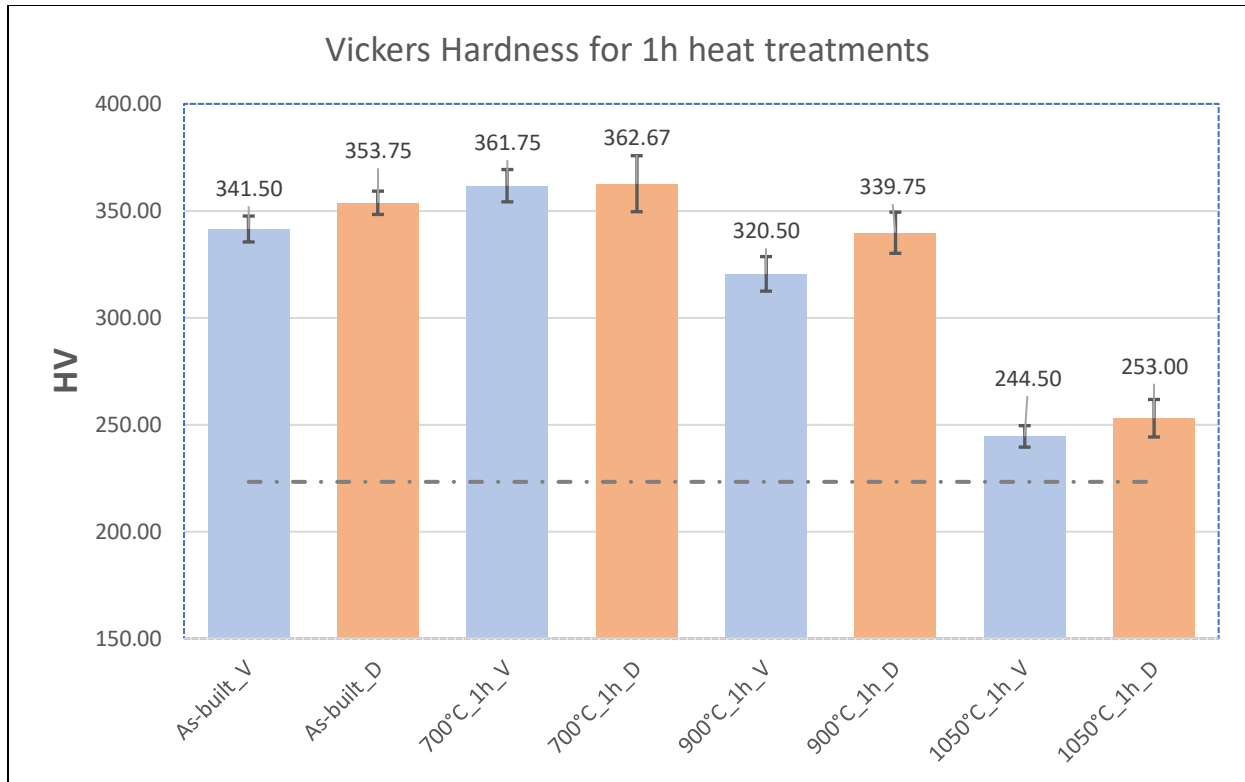


Figure 10: Microhardness (Vickers, 1000 gf, 30 s) of vertical and diagonal INC625 samples, for the as-built condition and three different heat-treated samples at 700 °C, 900 °C and 1050 °C for one hour each and air-cooled. The gray dashed line shows the hardness of wrought IN625 in non-heat-treated condition

### 3.2 Microstructure of the one-hour heat-treated specimen

Following the microhardness tests the specimen are etched and the microstructure is visualized with aid of an optical microscope. The crystal structure of the specimen and the lattice parameters are examined using XRD. Figure 11 shows the microstructure of the vertical as-built specimen, as well as the one-hour heat-treated specimen at 700 °C, 900 °C and 1050 °C, perpendicular to the built plate, which means in built direction (For magnified view see Appendix A to D). Figure 11 a)

shows the typical oval shaped melt pool boundaries for the as built L-PBF condition and some columnar grains, crossing the melt pool boundaries in built direction. The V shape of the melt pool boundaries is a well-known indicator for the Gaussian distribution of the laser energy, reaching the highest value in the center of the beam. [17] The columnar grains show the equiaxial grow in built direction. In figure 11 b) the 700 °C treated specimen is shown. The microstructure is very similar to the as built condition, even though it may be assumed that the irregular shaped white spots show even more formation of columnar grains in build direction. The columnar grains in build direction can be clearly seen for the 900 °C condition (Fig. 11 c)) in which no molten pool boundaries are visual anymore. After heating the sample to 1050 °C for one-hour, recrystallization, resulting in many fine grains, takes place, as can be seen in figure 11 d).



Figure 11: Microstructure of AM IN625 a) As-built condition, b) heat treated at 700°C for 1 hour, air cooled, c) heat treated at 900 °C for 1 hour, air cooled, d) heat treated at 1050 °C for 1 hour, air cooled.

Figure 12 shows the XRD results of the vertical as built specimen, figure 13 shows the XRD diagram of all four conditions. The austenitic structure can be seen in figure 12 and no other carbides or phases are found, even though they are often found in conventional manufactured In625. [12] This is due to the fast solidification time in the L-PBF process which leads to trapping of the solution elements in the Ni matrix. [13] It can be clearly seen that all four conditions have the same microstructure. No additional phases, like the intermetallic  $\gamma'$  [Ni<sub>3</sub>Al],  $\delta$  [Ni<sub>3</sub>Nb] or

$\gamma''$  [ $\text{Ni}_3\text{Nb}$ ] phase, are distinguishable in the pattern. According to Dinda et al. these particles are very fine in nature and hard to detect with XRD. [12]

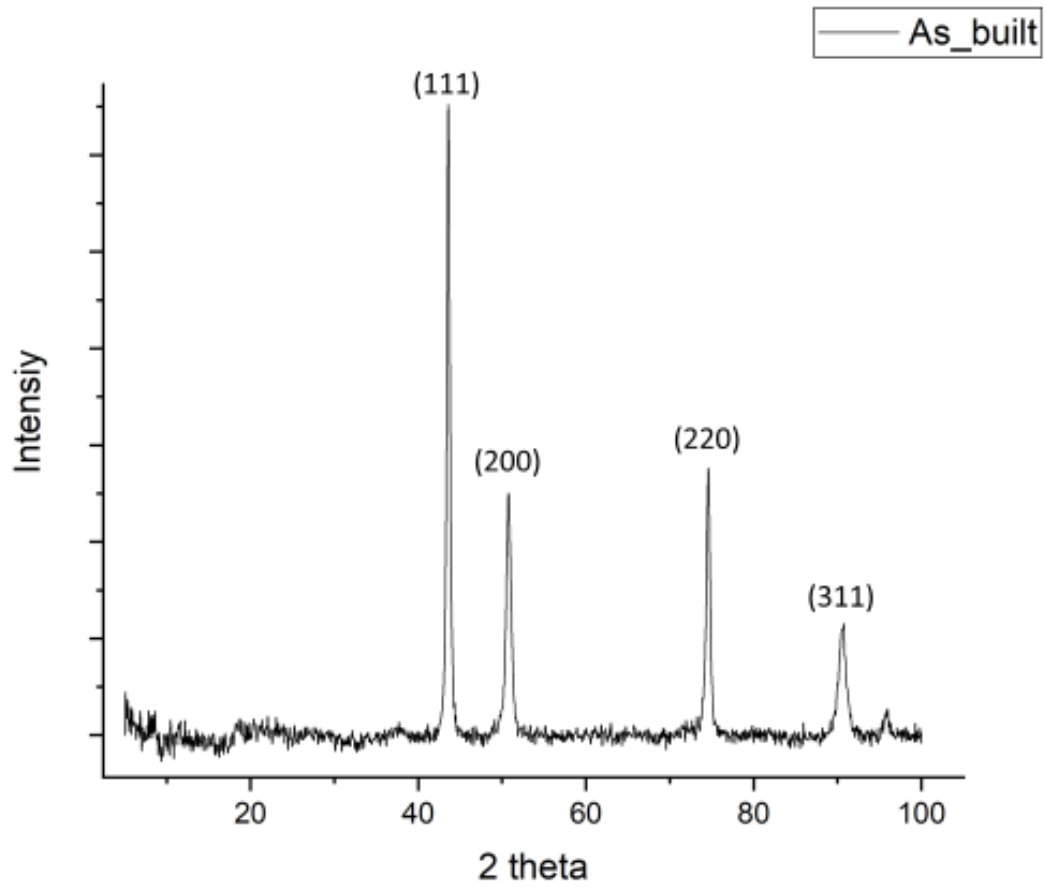


Figure 12: XRD results of the IN625 vertical as built specimen in the 2-theta range from 5° to 100°.

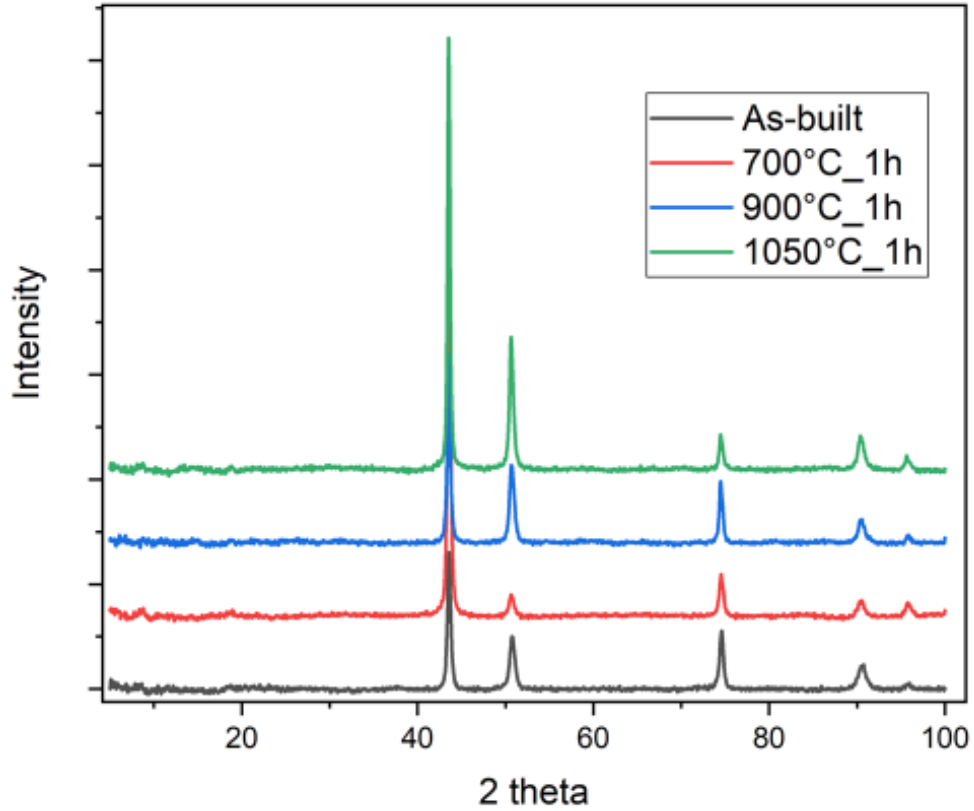


Figure 13: XRD results of the IN625 vertical specimen in the as built condition and heat treated for one hour at three different temperatures in the 2-theta range from  $5^\circ$  to  $100^\circ$ .

However, according to the literature, the change in lattice constants, calculated from the (200) peaks, can show the presence of precipitates indirectly. [12][13][19] According to Bragg's Law, the lattice parameter can be calculated using the following two equations:

$$(1) \quad 2d_{hkl}\sin\theta = n\lambda$$

$$(2) \quad d_{hkl} = a/\sqrt{h^2 + k^2 + l^2}$$

Table 3: Variation in lattice parameter calculated from (200) peak position for L-PBF manufactured IN625 in 4 different conditions for the one-hour heat treatment

Heat treatment	Lattice constant (Å)
<b>As built</b>	<b>3.5946</b>
<b>700°C_1h</b>	<b>3.5989</b>
<b>900°C_1h</b>	<b>3.5982</b>
<b>1050°C_1h</b>	<b>3.6018</b>

Even though manually taking the peak position to calculate the lattice constant might be quite error prone, figure 14 shows a clear peak shift for the (200) peak position which confirms the trend of lattice distortion. In addition, the lattice parameters are higher than that of the standard Ni-Cr FCC lattice (3.591 Å) which supports the statement.[18] The increase in the lattice parameter from the as built condition to the 700 °C heat-treated one can be explained by the dissolution of  $\gamma''$  in the  $\gamma$ -matrix, which means comparably large Nb atoms precipitate in the matrix, distorting the lattice. At temperatures above approximately 750 °C the orthorhombic  $\delta$ -phase is formed and decreases the lattice constant slightly, as the strengthening element Nb leaves the matrix. The volume fraction of  $\delta$  is very small and has therefore almost no influence on the lattice parameter. At the highest temperature of 1050 °C all strengthening elements are dissolved in the matrix, explaining the peak shift to the left and the rise in lattice parameter. The precipitation of the strengthening intermetallic  $\gamma''$ -phase in the matrix can also explain the increase in microhardness after heat treatment at 700 °C. [16] The further decrease in microhardness may be related to the dissolution of  $\gamma''$  in the matrix. Marchese et al. verify the precipitation of  $\gamma''$  and  $\delta$  with field emission scanning

electron microscopy (FESEM), and showed that after heat treating at 800 °C the precipitates are smaller than at 900 °C, therefore explaining the decrease in hardness. [16]

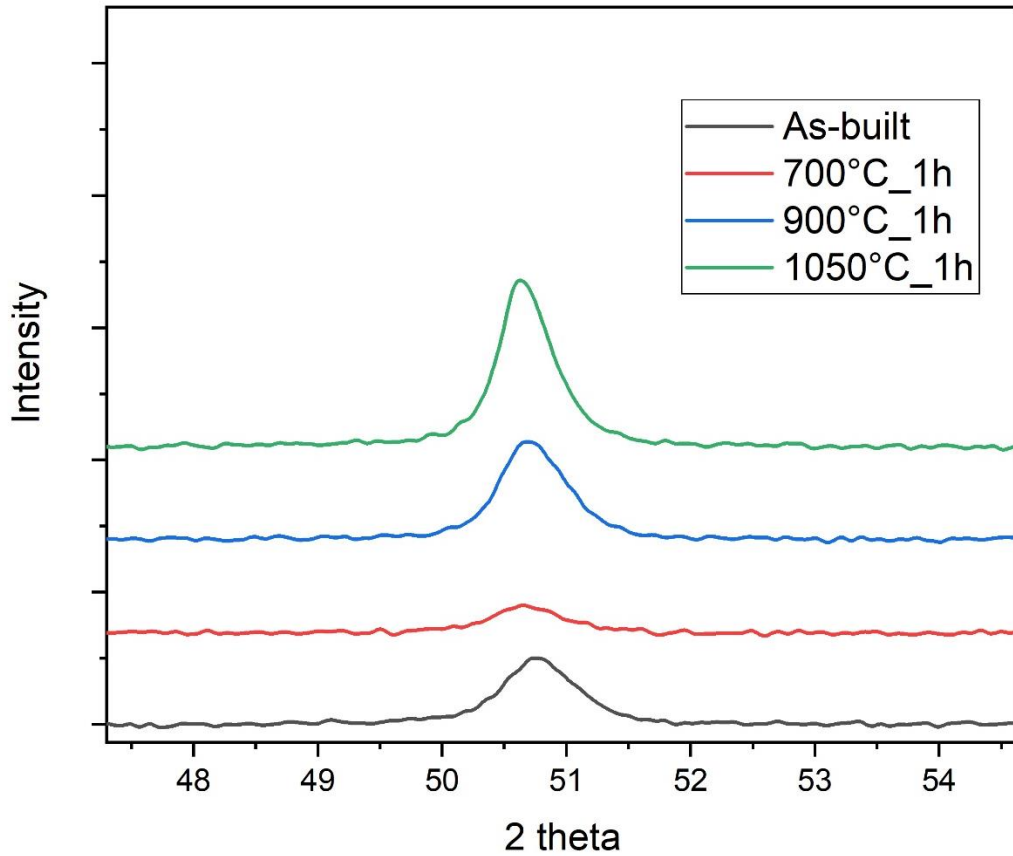


Figure 14: (200) Peak shift for L-PBF manufactured In625 in four different heat treatment conditions

### 3.3 Microhardness of the two-hour heat-treated specimen

Figure 15 shows the microhardness for the two hours heat treated specimen under the same temperatures as the previous ones. Again, there is no clear difference in microhardness between the diagonal and vertical built orientated samples. The as-built condition shows the highest

microhardness ( $HV\ 341.5 \pm 6.06$  and  $HV\ 353.75 \pm 5.45$  for vertical and diagonal built direction, respectively) which then decreases with increasing temperature. For the heat treatment at  $1050\text{ }^{\circ}\text{C}$  the microhardness again is much smaller compared to the other conditions.

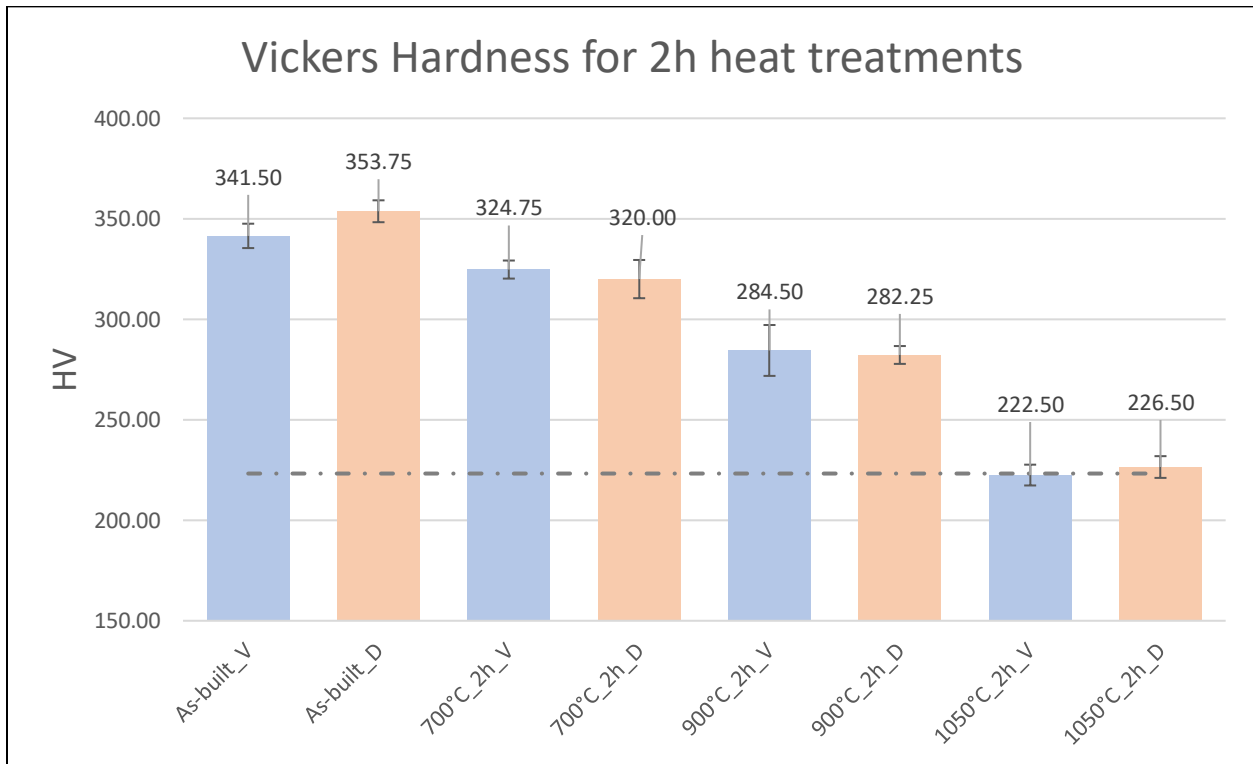


Figure 15: Microhardness (Vickers, 1000 gf, 30 s) of vertical and diagonal IN625 samples, for the as built condition and three different heat-treated samples at  $700^{\circ}\text{C}$ ,  $900^{\circ}\text{C}$  and  $1050^{\circ}\text{C}$  for two hours each and air-cooled. The gray dashed line shows the hardness of the wrought IN625 in non-heat-treated condition

### 3.4 Microstructure of the two-hour heat-treated specimen

The microstructures of the samples heat treated for two hours at  $700\text{ }^{\circ}\text{C}$ ,  $900\text{ }^{\circ}\text{C}$  and  $1050\text{ }^{\circ}\text{C}$  are shown in figure 16 a) to c), respectively. Again, in figure 16 a) the typical melt pool boundaries of the laser powder bed fusion process are recognizable, even though they are harder to detect

compared to the one-hour treatment. Figure 16 d) shows an enlarged view at higher magnification where red arrows indicate the melt pool boundaries. The green arrow shows exemplary the columnar dendrite growth in built direction, almost perpendicular to the built plate. In figure 16 b) no melt pool boundaries are recognizable anymore, only the dendrite structure is visible, and a slight widening of the dendrites can be seen. At the higher temperature of 1050 °C again recrystallization has taken over and the microstructure consists of many equiaxed grains.



Figure 16: Microstructure of AM INC625 a) heat treated at 700 °C for 2 hours, air cooled, b) heat treated at 900 °C for 2 hours, air cooled, c) heat treated at 1050 °C for 2 hours, air cooled, d) higher magnification of the 700°C heat treated sample, red arrows showing melt pool boundaries, green arrow shows grain growth in built direction.

The X-ray diffractogram of the two-hour heat-treated specimen is shown in figure 17. As for the one-hour heat-treatment, all samples show the same austenitic structure and no additional phases, like  $\gamma''$  or  $\delta$ , are distinguishable in the figure.

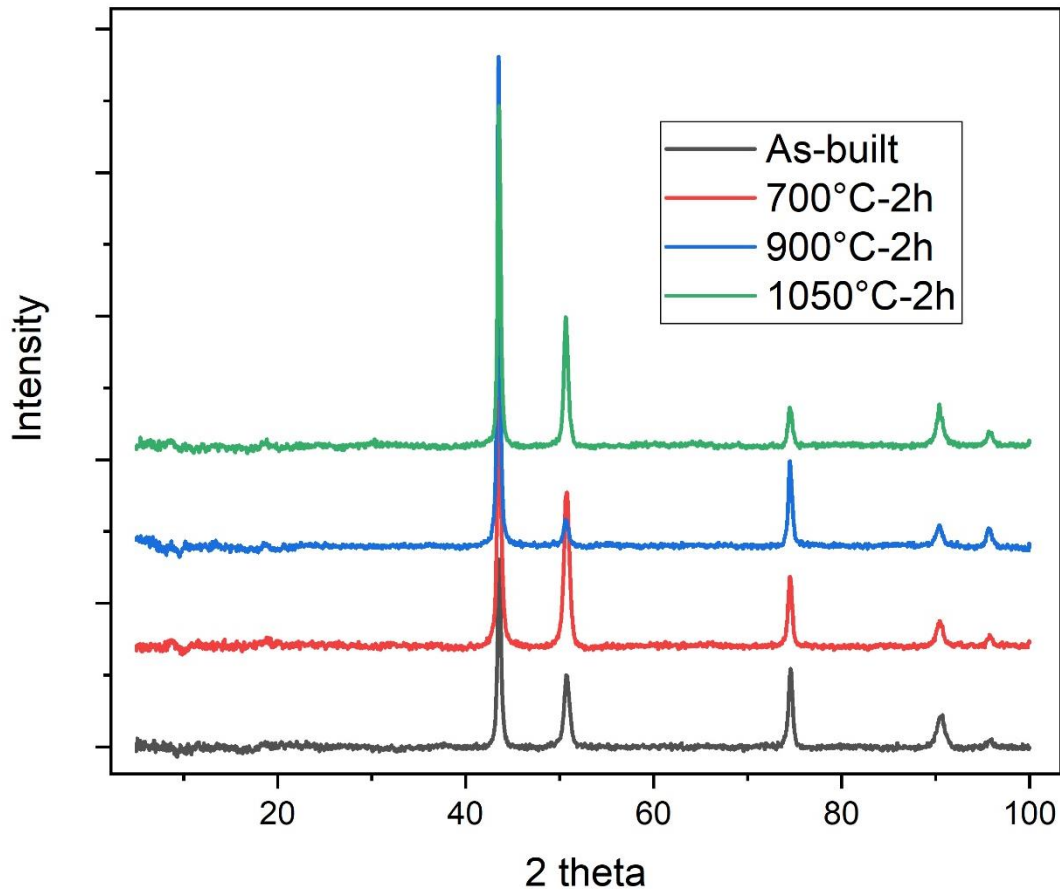


Figure 17: XRD results of the IN625 vertical specimen in the as built condition and heat treated for two hours at three different temperatures in the 2-theta range from 5° to 100°.

According to equation (1) and (2) the lattice parameter can be calculated accordingly and is given in table 4. After annealing at 700 °C for two hours the lattice constant increased slightly, which is as for the one-hour heat treatment explained by the dissolution of  $\gamma''$  into the matrix and therefore the re-entry of Nb atoms distorting the lattice. In contrast to the one-hour anneal at 900 °C, the

lattice constant increases even more for the two hour-anneal. According to Rao et al., who heat treated IN625 at 850 °C for one hour, the dissolution of the  $\gamma''$  into the matrix influences the lattice parameter strong compared to the precipitation of  $\delta$ . [19] Therefore, it might be possible that the two-hour heat treatment supported the dissolution of  $\gamma''$ . For the 1050 °C annealing an increase in lattice constant due to the dissolution of all strengthening elements into the matrix was expected. Yet, the opposite has happened. According to the literature, the presence of carbide precipitation from the matrix takes place at these elevated temperatures and can decrease the lattice distortion. [14]

Table 4: Variation in lattice parameter calculated from (200) peak position for L-PBF manufactured IN625 in 4 different conditions for the two-hour heat treatment

Heat treatment	Lattice constant (Å)
<b>As built</b>	<b>3.5946</b>
<b>700°C_2h</b>	<b>3.5953</b>
<b>900°C_2h</b>	<b>3.6004</b>
<b>1050°C_2h</b>	<b>3.5997</b>

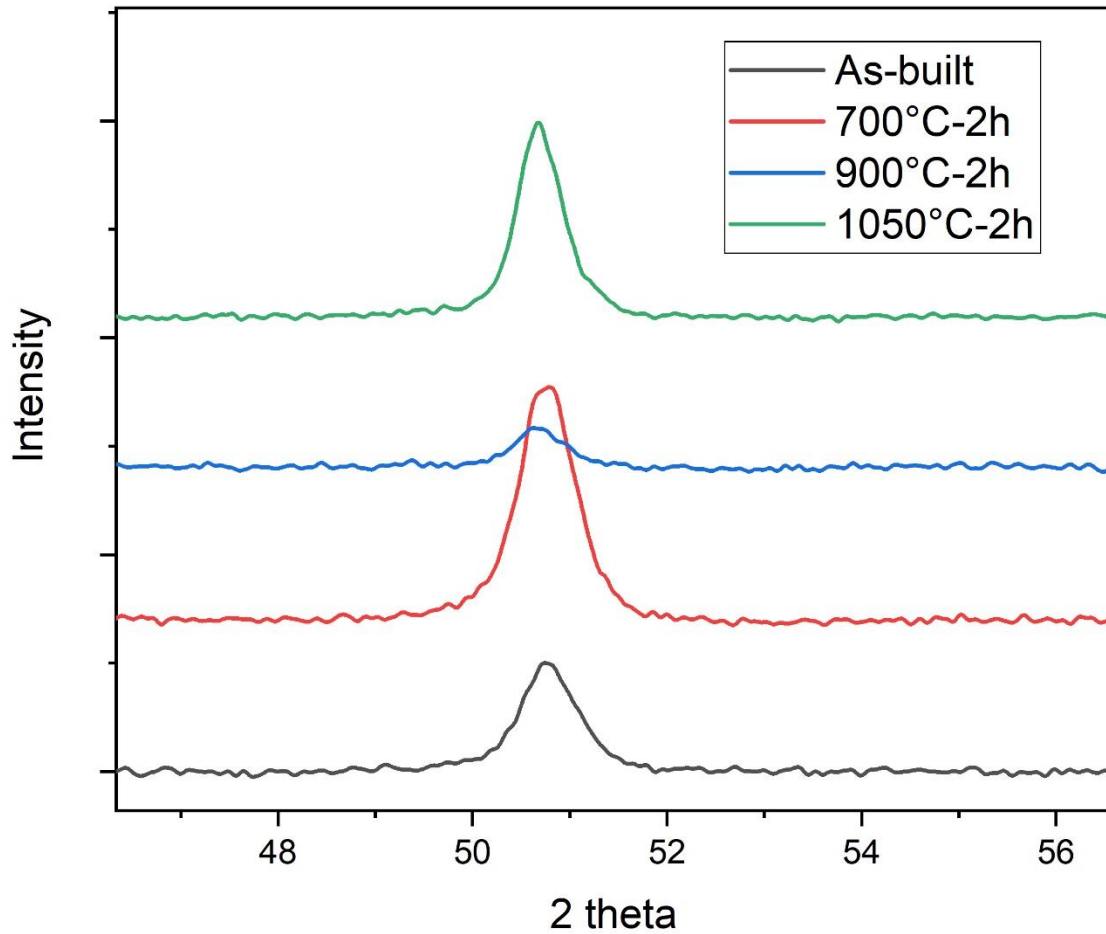


Figure 18: (200) Peak shift for L-PBF manufactured In625 in four different heat conditions for the two-hour heat-treated specimen

### 3.5 Comparison between both heat treatments

The microstructure of all specimens for the same heat-treatment condition is almost identical. The typical melt pool boundaries obtained from the characteristics of the laser get invisible at 900 °C, showing only columnar grains that are almost parallel to the build direction. After the sample was exposed to 1050 °C for either one or two hours the microstructure is completely recrystallized and

many equiaxed grains can be seen. For 1050 °C, the one hour and the two-hour specimen have the lowest microhardness due to grain coarsening and the complete relief of stress and dissolution of the strengthening phases. The dissolution of  $\gamma''$  in the matrix is expected to be the reason why the microhardness is lower after the 900 °C heat treatment than after the 700 °C heat treatment. Interestingly, after one-hour annealing at 700 °C an increase in hardness compared to the as built condition can be seen, while after two hours a slight decrease is recognized. Regarding the time-temperature-transformation diagram for IN625, that is shown in figure 4, at 700 °C several phases might be present. It should be noted, that the TTT diagram is not customized for additive or L-PBF processes and therefore the transformations probably occur after less time as explained in chapter 1. A decrease in hardness for longer annealing time leads to the assumption, that at this temperature with increasing time the amount of  $\gamma''$  decreases and/or with increasing time  $\delta$  precipitation takes place. However, while some researchers reported an increase in hardness with increasing time at 700 °C [12], others reported a decrease [13]. Therefore, it would be interesting for future projects to conduct several more heat treatments at temperatures close to 700 °C for several time intervals.

#### 4 Conclusion and outlook

Several samples of Inconel 625 have successfully been additively manufactured in vertical or diagonal orientation, using laser powder bed fusion. Microhardness measurements have revealed that for both orientations the HV value is almost identical. Heat treatments at 700 °C, 900 °C and 1050 °C have been conducted for one hour and two hours and microhardness as well as the microstructure have been evaluated to further understand the precipitation of the secondary phases, especially  $\delta$ -phase. As the secondary phases are hard to detect with XRD, changes in the lattice parameter for different annealing temperatures have been used to indirectly support the nature of precipitation. Whilst most of the hardness evolution over different temperature and time was successfully evaluated, some uncertainties remain. The precipitation of  $\gamma''$  in the matrix seems to harden the additively manufactured IN625, dissolution decreases the hardness and increases lattice distortion because of niobium atoms that reenter the matrix. The precipitation of  $\delta$  seems to have less influence on the lattice distortion as it is assumed to be present in only a very low amount, even though the decrease in microhardness at 900 °C and the increase of the lattice parameter after the two-hour treatment lead to the assumption that  $\delta$  precipitation occurred.

Most important, it has been shown that stress-relief heat treatments of L-PBF manufactured IN625 are very complex and should be well investigated before execution. Manufacturer suggested heat treatments, based on the nominal powder composition that do not include the microstructural changes due to the high cooling rates of some additive manufacturing processes may lead to  $\delta$ -phase formation and therefore might not only be ineffective but even detrimental to the parts performance and its mechanical properties.

For future projects, more heat treatments for longer times would be interesting to better understand the precipitation of  $\delta$ . In addition, the microhardness evolution between 600 °C and 800 °C needs to be further investigated for several time intervals. Examination with high resolution characterization techniques like scanning electron microscopy and transmission electron microscopy might be helpful to show the precipitation of secondary phases. After further understanding the  $\delta$ -phase precipitation, tensile tests would be interesting to further show the detrimental effect.

## References

- [1] Ngo, T.D., et al., Additive manufacturing (3D printing): A review of materials, methods, applications and challenges. *Composites Part B: Engineering*, 2018. 143: p. 172-196.
- [2] Sames, W.J., et al., The metallurgy and processing science of metal additive manufacturing. *International Materials Reviews*, 2016. 61(5): p. 315-360.
- [3] Calignano, F., Investigation of the accuracy and roughness in the laser powder bed fusion process. *Virtual and Physical Prototyping*, 2018. 13(2): p. 97-104.
- [4] Floreen, S., G.E. Fuchs, and W.J. Yang, The metallurgy of alloy 625. *Superalloys*, 1994. 718(625): p. 13-37.
- [5] Lass, E.A., et al., Formation of the Ni<sub>3</sub>Nb  $\delta$ -phase in stress-relieved Inconel 625 produced via laser powder-bed fusion additive manufacturing. *Metallurgical and Materials Transactions A*, 2017. 48(11): p. 5547-5558.
- [6] Zhang, F., et al., Homogenization kinetics of a nickel-based superalloy produced by powder bed fusion laser sintering. *Scripta materialia*, 2017. 131: p. 98-102.
- [7] Wilhelm M. Direktes selektives laser sintern einkomponentiger metallischer werkstoffe. Dissertation,(RWTH Aachen). 1999.
- [8] Kreitchberg A, Brailovski V, Turenne S. Effect of heat treatment and hot isostatic pressing on the microstructure and mechanical properties of Inconel 625 alloy processed by laser powder bed fusion. *Materials Science and Engineering: A*. 2017;689:1-10.
- [9] General Electric, Online, 06/14/2010  
<https://www.ge.com/additive/de/who-we-are/concept-laser>

- [10] ASTM A. Standard test method for microindentation hardness of materials. ASTM International West Conshohocken. 2011.
- [11] O'Brien MJ. Development and qualification of additively manufactured parts for space. *Optical Engineering*. 2019;58(1):010801.
- [12] Dinda G, Dasgupta A, Mazumder J. Laser aided direct metal deposition of Inconel 625 superalloy: Microstructural evolution and thermal stability. *Materials Science and Engineering: A*. 2009;509(1-2):98-104.
- [13] Li S, Wei Q, Shi Y, Zhu Z, Zhang D. Microstructure characteristics of Inconel 625 superalloy manufactured by selective laser melting. *Journal of Materials Science & Technology*. 2015;31(9):946-52.
- [14] Nguejio J, Szmytka F, Hallais S, Tanguy A, Nardone S, Martinez MG. Comparison of microstructure features and mechanical properties for additive manufactured and wrought nickel alloys 625. *Materials Science and Engineering: A*. 2019;764:138214
- [15] Shoemaker LE. Alloys 625 and 725: trends in properties and applications. *Superalloys*. 2005;718(625):409-18.
- [16] Marchese G, Lorusso M, Parizia S, Bassini E, Lee J-W, Calignano F, et al. Influence of heat treatments on microstructure evolution and mechanical properties of Inconel 625 processed by laser powder bed fusion. *Materials Science and Engineering: A*. 2018;729:64-75.
- [17] Marchese G, Garmendia Colera X, Calignano F, Lorusso M, Biamino S, Minetola P, et al. Characterization and comparison of Inconel 625 processed by selective laser melting and laser metal deposition. *Advanced Engineering Materials*. 2017;19(3):1600635.

- [18] Li C, White R, Fang X, Weaver M, Guo Y. Microstructure evolution characteristics of Inconel 625 alloy from selective laser melting to heat treatment. *Materials Science and Engineering: A*. 2017;705:20-31.
- [19] Rai SK, Kumar A, Shankar V, Jayakumar T, Rao KBS, Raj B. Characterization of microstructures in Inconel 625 using X-ray diffraction peak broadening and lattice parameter measurements. *Scripta materialia*. 2004;51(1):59-63.
- [20] Stoudt MR, Lass E, Ng DS, Williams ME, Zhang F, Campbell CE, et al. The influence of annealing temperature and time on the formation of  $\delta$ -phase in additively-manufactured Inconel 625. *Metallurgical and Materials Transactions A*. 2018;49(7):3028-37.

Appendix A: Microstructure of specimen As-built\_V



Appendix B: Microstructure of specimen 700°C\_1h\_V



Appendix C: Microstructure of specimen 900°C\_1h\_V



Appendix D: Microstructure of specimen 1050°C\_1h\_V



Appendix E: Microstructure of specimen 700°C\_2h\_V



Appendix F: Microstructure of specimen 900°C\_1h\_V



Appendix G: Microstructure of specimen 1050°C\_2h\_V

